

Detection of afterglow emission up to 100 GeV through a stacking analysis of gamma-ray bursts

SHI CHEN,^{1,2} QIANG YUAN,^{3,4} YI-QING GUO,^{2,5,6} BEN-ZHONG DAI,¹ HE GAO,^{7,8} AND
BING ZHANG^{9,10}

¹*School of Physics and Astronomy, Yunnan University, Kunming 650091, P. R. China*

²*State Key Laboratory of Particle Astrophysics, Institute of High Energy Physics, Chinese Academy of Sciences, Beijing 100049, P. R. China*

³*Division of Dark Matter and Space Astronomy, Purple Mountain Observatory, Chinese Academy of Sciences, Nanjing 210023, P. R. China; yuanq@pmo.ac.cn*

⁴*School of Astronomy and Space Science, University of Science and Technology of China, Hefei 230026, P. R. China*

⁵*University of Chinese Academy of Sciences, Beijing 100049, P. R. China*

⁶*TIANFU Cosmic Ray Research Center, Chengdu 610000, P. R. China; guoyq@ihep.ac.cn*

⁷*School of Physics and Astronomy, Beijing Normal University, Beijing 100875, P. R. China*

⁸*Institute for Frontiers in Astronomy and Astrophysics, Beijing Normal University, Beijing 102206, P. R. China*

⁹*The Hong Kong Institute for Astronomy and Astrophysics, University of Hong Kong, Pokfulam Road, Hong Kong 999077, P. R. China*

¹⁰*Department of Physics, University of Hong Kong, Pokfulam Road, Hong Kong 999077, P. R. China*

ABSTRACT

High-energy gamma-ray ($> \text{GeV}$) emission of gamma-ray bursts (GRBs) is very important in probing the jet evolution and particle acceleration of GRBs. The observations of high-energy photons are limited except for a few very bright GRBs, hindering precise measurements of the spectral and temporal evolutions of GRBs. Here we report the detection of high-energy gamma-ray emission up to 100 GeV with Fermi-LAT using a stacking analysis of a collection of 330 GRBs. High significance detection of the emission has been found, and the precise light curves and energy spectra can be measured. The light curves and time-resolved spectra of the sub-sample of 220 LAT individually detected GRBs can be well explained by the standard afterglow emission from a population of GRBs with both synchrotron and synchrotron self-Compton mechanisms, assuming a distribution of initial Lorentz factors. However, the emission of the relatively weak sample of the 110 LAT individually undetected GRBs cannot be well reproduced in the same framework, indicating the existence of possible energy injection effect in the GeV band for the first time. The observations hence provide new insights in understanding the high-energy emission of GRBs.

Keywords: High energy astrophysics — Non-thermal radiation sources — Gamma-ray bursts

GRBs are among the most extreme cosmic explosions, serving as unique laboratories for studying relativistic jets and particle acceleration under extreme conditions (Zhang & Meszaros 2004; Kumar

& Zhang 2015). While the prompt emission of GRBs is expected to be produced by internal shocks within the jet, the long-lasting afterglow arises from external shocks due to the jet interaction with the circum-burst medium which then produces wide-band emission via synchrotron and the inverse Compton scattering processes (Sari & Esin 2001; Zhang et al. 2011). The high-energy emission of GRBs is usually dominated by this afterglow component (Ajello et al. 2019), and thus plays a crucial role in constraining the jet parameters, magnetic field properties, and the maximum accelerated energies for GRBs (Kumar & Zhang 2015; Acciari et al. 2019a). However, observations of high-energy emission are rare, due to the limited effective area of space detectors and the challenges of groundbased observations (small field-of-view or high background). Currently, only a few very bright GRBs have been detected to have enough photons enabling a good description of the spectra and light curves by the space detector Fermi Large Area Telescope (LAT) (Ajello et al. 2019; Abdollahi et al. 2022) and groundbased experiments (Acciari et al. 2019b; Abdalla et al. 2021; Cao et al. 2023). This situation cannot be easily improved in the near future for individual GRB observations. A stacking analysis for a population of sources may effectively overcome this issue, as has been done for pulsars (McCann 2015), galaxy clusters (Huber et al. 2013), and the prompt phase of GRBs (Ackermann et al. 2016)¹.

In this work we employ the stacking technique to study the high-energy gamma-ray emission from a sample of GRBs using the data recorded by the Fermi-LAT instrument (Atwood et al. 2009). From August, 2008 to December, 2024, a total of 222 GRBs have been reported by Fermi-LAT, triggered by either the LAT or the Gamma-ray Burst Monitor (GBM) (Meegan et al. 2009). In our analysis, 220 GRBs out of the 222 ones, excluding two bright GRBs 130427A (Ackermann et al. 2014) and 221009A (Axelsson et al. 2025), are used. These LAT individually detected GRBs (“LAT detected GRBs” for short) exhibit diverse properties of energy distributions and other statistical properties (Ajello et al. 2019). For most of these GRBs the numbers of high-energy photons are very few, for which the spectra and light curves can not be obtained and thus the high-energy behaviors of the emission can not be well extracted. We also compile a sample of 110 GRBs which were triggered by Swift/BAT (Donato et al. 2012) and not detected by Fermi-LAT (referred to as “LAT individually undetected GRBs” and “LAT undetected GRBs” for short), with a filtering condition that at least one event exists within 1° radius of each GRB. Such a sample represents the faintest end of GRBs can be studied with the current Fermi-LAT detector.

We use the official Fermi Science Tools provided by the Fermi Science Support Center (FSSC) to analyze the data. Photons in the 0.1 – 100 GeV band from a $10^\circ \times 10^\circ$ region centered on the location of each GRB for a time window of 50000 seconds after the trigger have been stacked. The background contains emission from the Galactic diffuse background, the isotropic diffuse background, and sources from the 4FGL catalog (Abdollahi et al. 2022) (see Appendix A for more details). Figure 1 shows the significance maps of the 220 LAT detected sample (panel **a**) and the 110 LAT undetected sample (panel **b**). Note that, for the 110 LAT undetected sample, the number of photons is limited and only significant detection in the 1 – 10 GeV is found and hence the significance map is derived using the 1 – 10 GeV events. Significant detection of both samples can be found, with significance of 99.7σ for the 220 LAT detected sample and 17.9σ for the 110 LAT undetected sample (see Appendix B for the calculation of the significance). To check that whether these excess photons indeed come

¹ Note that in Ackermann et al. (2016) 79 GRBs with Swift localizations were investigated with a stacking technique. However, no detailed spectral and temporal behaviors of the GRB sample were studied.

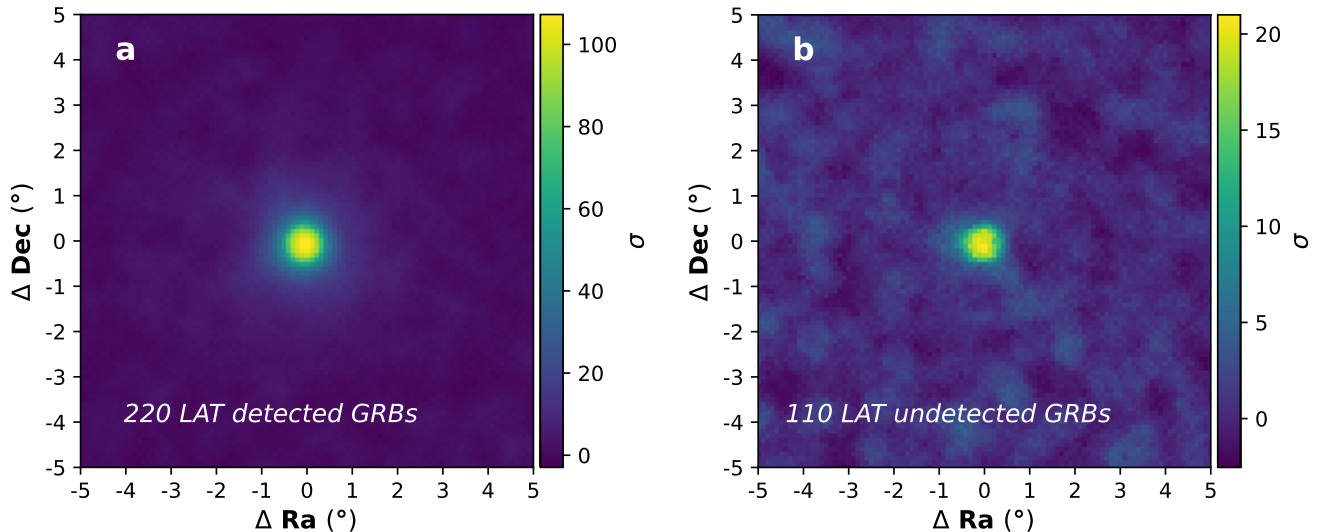


Figure 1. The $10^\circ \times 10^\circ$ significance maps of the stacked GRBs smoothed with a 0.4° Gaussian kernel. For each GRB, photons in the region of the same size centered on its trigger position within a time duration from the trigger time T_0 to $T_0 + 50,000$ s are collected. Panel **a** is for the 220 LAT detected GRBs with photon energies from 0.1 to 100 GeV, and panel **b** is for the 110 LAT undetected GRBs with energies from 1 to 10 GeV.

from GRBs, we derive the one-dimensional angular distribution of the photons after subtracting the background, for the 220 LAT detected sample. The results in different energy bands can be modelled with Gaussian functions, as shown in Figure A2 of Appendix. The angular distributions are consistent with the point spread function (PSF), as indicated by the standard pointlike source of the crab (including both the pulsar and nebula), except in the lowest energy band where different spectral shapes may result in slightly different PSFs.

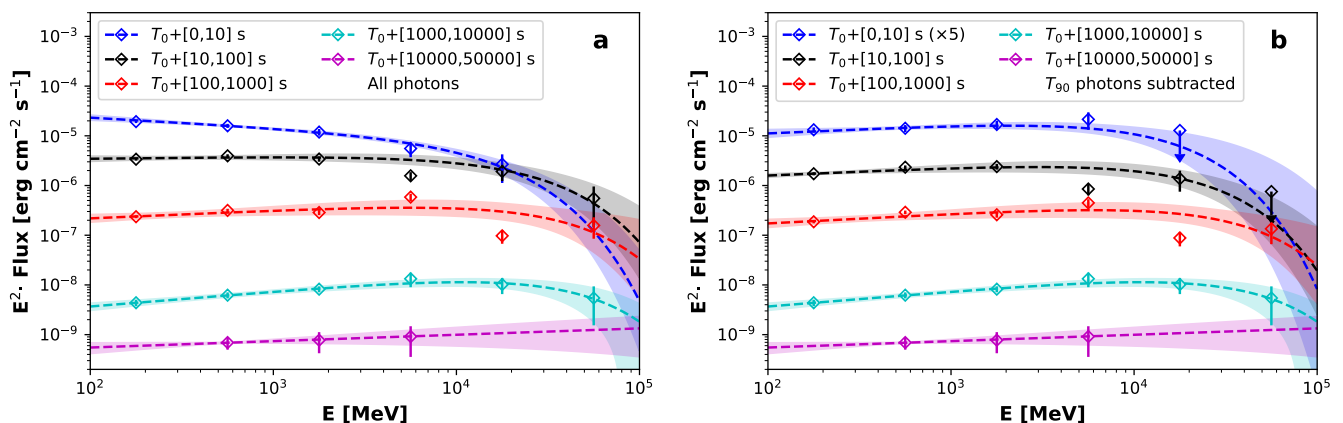


Figure 2. SEDs at different time for the 220 LAT detected GRBs. Five time intervals are adopted: $T_0 + [0, 10]$ s, $T_0 + [10, 100]$ s, $T_0 + [100, 1000]$ s, $T_0 + [1000, 10000]$ s, and $T_0 + [10000, 50000]$ s. Panel **(a)** shows the results obtained for all photons, and panel **(b)** shows the results after removing photons within T_{90} of each GRB. Dashed lines and shaded bands show the best-fitting results and the $\pm 1\sigma$ uncertainty bands with an ECPL model.

We extract photons in different time windows after their trigger time (T_0), and derive the spectral energy distributions (SEDs) at different time. The results of the 220 LAT detected GRBs are shown in Figure 2. One can see that if all the photons are taken into account (panel **a**), the spectra experience a clear evolution from soft at early time to hard at late time. However, there might be contribution from prompt emission at early time. To reduce the possible impacts from the prompt emission, we show in panel (**b**) the SEDs after subtracting photons within T_{90} of each GRB, where T_{90} is defined as the time interval containing 90% of the γ -ray photons during the burst phase. The SEDs appear similar among different time. We fit the SEDs with an exponential cutoff power-law (ECPL) model, $\phi(E) \propto E^{-\alpha} \exp(-E/E_{\text{cut}})$. The evolution of spectral indices with time is given in Figure A3 (panel **a**). We can see that if the photons within T_{90} are removed, the spectral index keeps roughly a constant of $\alpha \sim 1.8$. Including the photons within T_{90} results in softer spectra at early time (Ravasio et al. 2024). The cutoff energy shows a trend of increase with time (panel **b** of Figure A3), which may indicate that the high-energy component from the inverse Compton scattering process becomes more and more important at later time (see below discussion on the modeling).

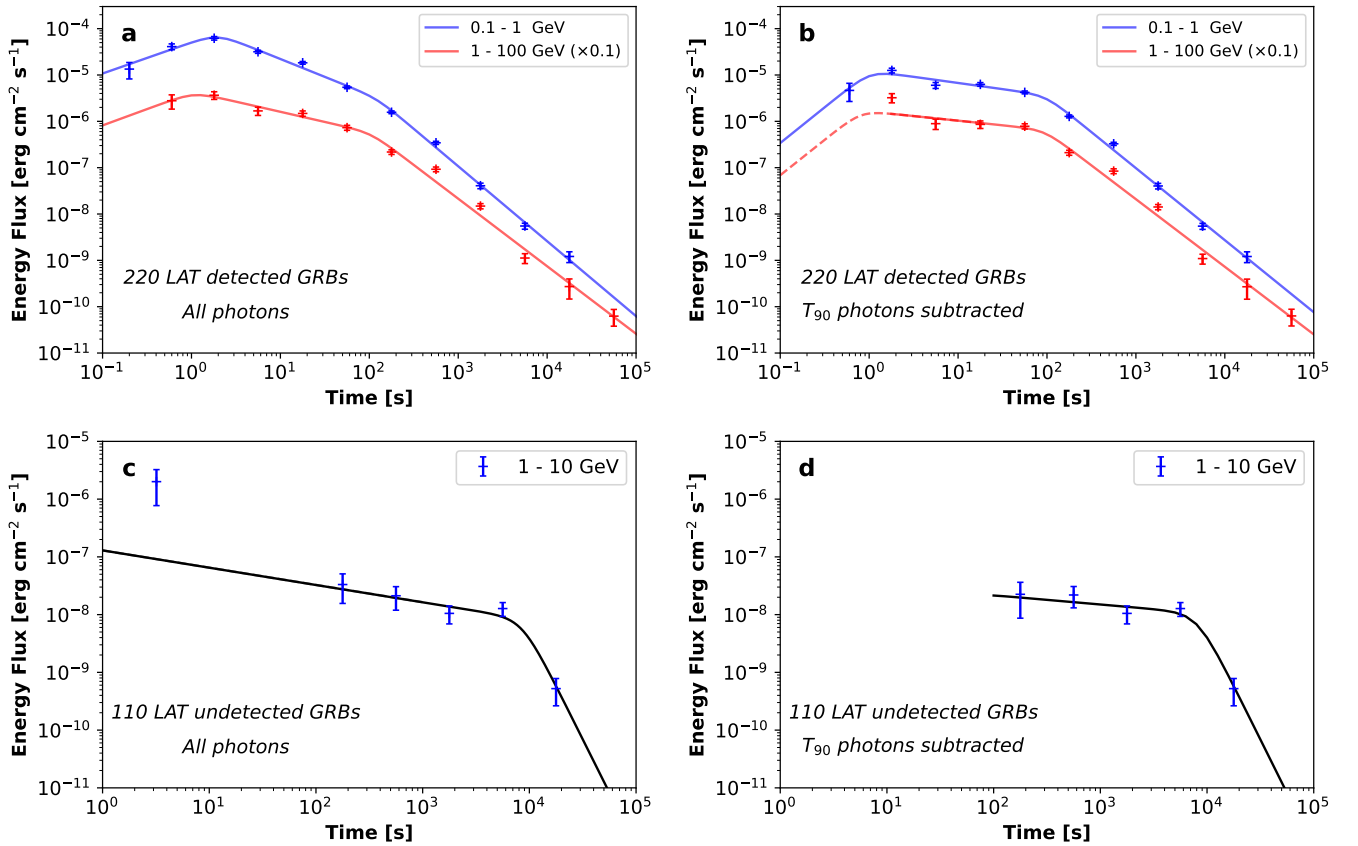


Figure 3. Light curves of the stacked GRBs and the corresponding fitting results. The light curves for all photons and for those with T_{90} photons subtracted are shown in panels **a** and **b** for the 220 LAT detected GRBs, and in panels **c** and **d** for the 110 LAT undetected GRBs, respectively. All light curves are fitted using a multi-piece power-law model, with fitting parameters being given in Table A1.

The light curves of the two samples are shown in Figure 3, for all photons (panels **a** and **c**) and photons within T_{90} subtracted (panels **b** and **d**). For the 220 LAT detected GRBs, the results in

two energy bands, 0.1 – 1 GeV and 1 – 100 GeV, are presented (panels **a** and **b**), while for the 110 LAT undetected GRBs the results in 1 – 10 GeV are shown (panels **c** and **d**). The light curves of the 220 LAT detected GRBs can be fitted with three-piece power-law functions, as shown by solid lines in the figure. For the case with all photons, the light curves show a rise at the early time with a slope of ~ 0.7 , followed by a shallow decay (with decay slope of $-0.8 \sim -0.4$) after a few seconds and a steep decay (with decay slope of ~ -1.5) at about 100 s after the trigger. The slopes of the shallow decay phase vary with energies, which may be due to the prompt emission contamination. If we remove the photons within T_{90} , the light curves of different energy bands become similar with each other. In this case, the broken power-law evolution behaviors are also visible, but the rising phase becomes less clear due to limited number of photons. The slopes of the shallow decay phase are about $-0.2 \sim -0.3$, which evolve to the steep decay phase with slope of ~ -1.5 at ~ 100 s after the trigger. For the 110 LAT undetected GRBs, a two-piece power-law behavior can be seen, but the rising phase as shown in the 220 LAT detected sample cannot be detected. The slope of the shallow decay is again about $-0.2 \sim -0.3$, followed by a steep decay with slope of -3.7 but with relatively large uncertainty. The break time from the shallow decay to the steep decay is different for the two samples (~ 100 s for the 220 GRBs and $\sim 10^4$ s for the 110 GRBs), which we expect may be due to different Lorentz factors of the jets and/or late-time energy injection effect for the two samples.

In the standard afterglow model of GRBs (Sari et al. 1998; Kumar & Duran 2010), the slow rise phase may correspond to the coasting stage that the forward shock sweeps up the ambient medium before significant deceleration. After that, the jet enters the deceleration phase, and the light curve starts to decay. With the continuous deceleration of the jet, when the Lorentz factor of the jet becomes smaller than $1/\theta_j$ where θ_j is the half-opening angle of the jet (known as the jet break (Rhoads 1999)), a steeper decay of the emission is expected. Eventually, the jet becomes non-relativistic and enters the Newtonian evolution stage. Depending on the specific parameters, the evolution slopes of the light curves differ case by case (Dermer et al. 2000; Gao et al. 2013). The results obtained in this work likely show the expected evolution of the standard afterglow model. However, a more complicated situation here is the cumulative effect of many GRBs with diverse properties.

We model the SEDs and light curves with the forward shock model of the GRB afterglow. In this model, the propagation of relativistic jets in the circum-burst medium produces forward shocks which accelerate high-energy electrons. These energetic electrons then produces multi-wavelength emission through synchrotron and/or inverse Compton emission. In the energy band of Fermi-LAT, both the synchrotron emission and the synchrotron self-Compton (SSC) emission are relevant (Zhang & Meszaros 2001; Wang et al. 2019). The parameters of the GRBs in our sample should be different from one to another. One of the major parameter affecting the afterglow evolution is expected to be the initial Lorentz factor of the jet, Γ_0 . The initial kinetic energy (E_0) of the jet which affects the normalization of the emission is also a highly relevant parameter. Following the results of Liang et al. (2010), we assume that the initial Lorentz factor has a log-normal distribution, with the mean value of $\log(\Gamma_0) = 2.37$ and the width of 0.26. For the 220 LAT detected sample, which are expected to be more powerful, E_0 is taken to be 4×10^{53} erg, Γ_0 is restricted in the range of [130, 800], and the jet opening angle is assumed to be 0.8° . For the 110 LAT undetected sample, E_0 is assumed to be 4×10^{52} erg, Γ_0 is restricted in the range of [60, 250], and the jet opening angle is taken to be 4° . The initial Lorentz factor and the kinetic energy follows also the correlation of $\Gamma_0 \sim E_0^{0.25}$ (Liang et al. 2010), as shown in Figure A4 of the Appendix. The other parameters are fixed to be the same

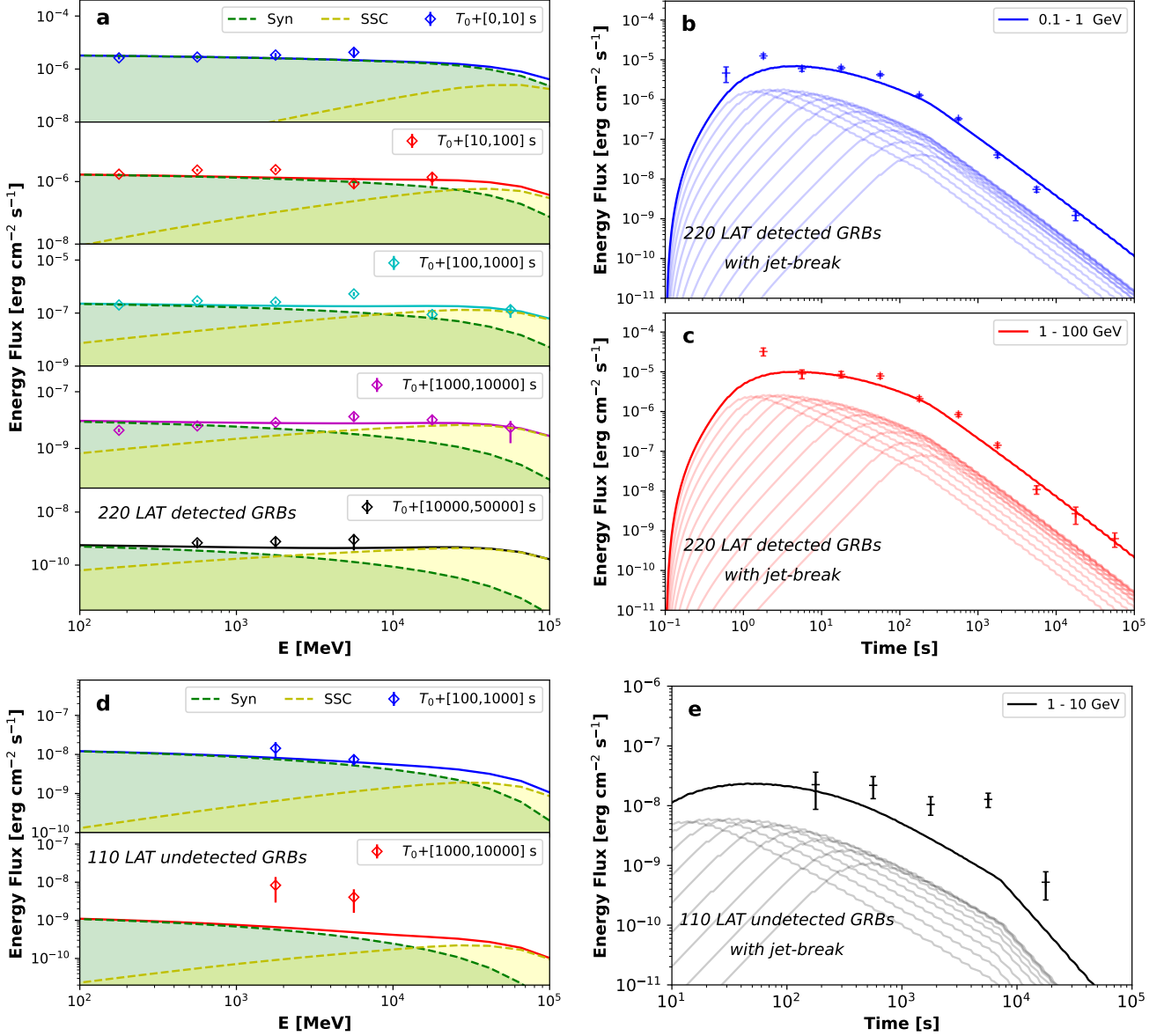


Figure 4. Stacked SEDs and light curves from GRB population with log-normal initial Lorentz factor distribution. Panels **a**, **b** and **c** present the stacked model SEDs and light curves for the high initial Lorentz factor ($\Gamma_0 \sim 130 - 800$) populations, corresponding to the 220 LAT detected GRBs. Panels **d** and **e** show the corresponding stacked model SEDs and light curves for the low initial Lorentz factor ($\Gamma_0 \sim 60 - 250$) populations, which are derived for the 110 LAT undetected GRBs.

for all GRBs (see Appendix E for details). The stacked model results of the SED and light curves are given in Figure 4.

The model successfully reproduces the three-segment power-law evolution of the light curves for the 220 LAT detected GRBs. The emission reaches a peak after the rising phase, when the jet starts to decelerate. The peak time is related with the initial Lorentz factor as $t_{\text{peak}} \propto \Gamma_0^{-8/3}$. Therefore, the shallow decay phase we observe can be ascribed to the superposition of various shallow decay curves for the population of GRBs. The shallow decay slope of $-0.2 \sim -0.3$ depends on the distribution of

the initial Lorentz factor, and is flatter than the shallow decay phase of individual GRB. The light curve enters the steep decay phase after the jet break of the GRB with the latest t_{peak} . The jet break is necessary to reproduce the steep decay phase of the light curve. As can be seen in Figure A4, the data cannot be well accounted for without the jet break.

For the 110 LAT undetected GRBs, the model prediction shows some tension with the observations. It is interesting to note that the break time from the shallow decay to the steep decay is about 10^4 s, just consistent with the durations of X-ray plateaus of canonical GRBs (Zhang et al. 2006). For the GeV bright GRBs detected by Fermi-LAT, the X-ray light curves usually show single power-law decay without clear plateaus (Yamazaki et al. 2020). This is consistent with the results obtained here, i.e., long-lasting emission exists in the sample with weaker GeV emission. As a consistency test, we compile the available X-ray afterglow data of the two samples studied in this work, and find that for the 110 LAT undetected sample the X-ray light curves indeed tend to favor the existence of energy injection more than the 220 LAT detected sample (see Appendix F). Our results likely give the first detection of GeV counterparts of canonical GRBs with X-ray plateaus, and indicate that later energy injection from the central engine may take effect in shaping the evolution of γ -ray afterglow for the class of weak GRBs.

The SEDs can be roughly explained by the model for the 220 LAT detected sample, but show excesses for the 110 LAT undetected sample. Both the synchrotron and SSC components contribute to the time-resolved spectra and light curves, suggesting that the transition of radiation mechanisms occurs in the $O(10)$ GeV γ -ray band. The energy flux of the SSC component is comparable to the synchrotron component, which is very useful in constraining the energy allocation of GRB jets (Joshi & Razzaque 2021) and the contribution to the extragalactic γ -ray background from the GRB population (Casanova et al. 2007). Time evolution of these two components can be seen: the synchrotron component dominates the emission at early time, and with the increase of time the SSC component gradually becomes more and more important, especially in the high energy band. This can also explain the increase trend of the cutoff energy as obtained in the phenomenological ECPL fitting of the SEDs (see Figure A3 of the Appendix).

The results of this analysis show that the high-energy afterglow emission of GRBs should generally exist up to 100 GeV. However, for single event the number of photons is usually very limited for space detectors and the detection of such emission is very difficult. With the stacking technique, we can reach the high significance detection of such emission and precisely characterize the spectral and temporal properties. The results verify the canonical afterglow emission due to interactions of GRB jets with the circum-burst medium (Ghisellini et al. 2010). It is also possible that there is energy injection signature in the GeV γ -ray band for the relatively weaker sample. The jet-break like feature has been observed on the light curves, which can provide useful constraints on the jet dynamics. Although it is not clear to what energy the prompt emission can extend, the SEDs indicate that possible prompt emission up to several GeV exists in the data. It is currently challenging to decompose the prompt emission and the afterglow within the bursting phase (T_{90}). Future high-energy γ -ray observations with bigger effective area (Pan et al. 2024) may better address this issue.

ACKNOWLEDGEMENTS

This work is supported by the National Natural Science Foundation of China (Nos. 12321003, 12220101003, 12263007, and 12233006), the Project for Young Scientists in Basic Research of the

Chinese Academy of Sciences (No. YSBR-061), and the High-level Talent Support Program of Yunnan Province.

APPENDIX

A. STACKING ANALYSIS OF THE FERMI-LAT DATA

From August, 2008 to December, 2024, 222 GRBs have been detected by Fermi-LAT, with detailed information being available through the GRBweb². We use the Fermitools from the Fermi Science Support Center (FSSC) to analyze the data. To enable a good statistics, the `SOURCE` class events with reconstruction version of `P8R3_SOURCE_V3` have been adopted. For each GRB, we select events within a region of interest (ROI) of 10° centered on the location of the burst. Both `FRONT` and `BACK` events are adopted. The time range is chosen to be 50000 s after the trigger time T_0 , and the energy range is from 100 MeV to 100 GeV. The maximum zenith angle is set to be 90° to filter out the background from the Earth's limb. The event selection further includes filters (`DATA_QUAL>0`) && (`LAT_CONFIG==1`) to ensure good quality of the data.

A count map is derived for each GRB. By stacking the count maps of all 220 GRBs excluding the very bright two GRBs 130427A and 221009A, we obtain a total count map. This map includes signal events from GRBs, and background emission from the isotropic gamma-ray background (IGRB) (Ackermann et al. 2015), the diffuse Galactic background (Ackermann et al. 2012a), and sources (Abdollahi et al. 2022) in the ROI.

In addition, a sample of Swift/BAT triggered GRBs but not detected by Fermi-LAT individually from the same period of August, 2008 to December, 2024 has also been collected. We further require that there is at least one photon like event within 1° radius of each GRB after the above event selections. It turns out that 110 GRBs remain in this sample.

B. LIKELIHOOD FITTING

We apply the likelihood analysis on each GRB. Usually the binned likelihood method is adopted, unless for very short time bins (less than 200 s) where the number of events is very limited and the unbinned likelihood analysis is adopted. The model includes the signal from the GRB, the sources in the ROI from the 4FGL catalog (Abdollahi et al. 2022) (`gll_psc_v32.fit`), and the diffuse backgrounds³. For the diffuse Galactic emission we use the template `gll_iem_v07.fits`, and for the isotropic background we use the spectral model `iso_P8R3_SOURCE_V3_v1.txt`. The background emission (including both the diffuse backgrounds and field sources) for each GRB is obtained and subtracted from the data. Excess emission from the sample of GRBs can be obtained. The significance map for 220 GRBs observed by LAT and 110 GRBs not recorded by LAT is shown in Figure 1.

Summing the logarithmic likelihood values together, we get the total Test Statistic (TS) value, defined as $TS = 2(\ln \mathcal{L} - \ln \mathcal{L}_0)$, where \mathcal{L} and \mathcal{L}_0 represent the likelihood values with and without target GRBs, as 10181.8 for the 220 LAT detected GRBs across 0.1 – 100 GeV band from T_0 to $T_0 + 50,000$ seconds. For the 110 LAT undetected GRBs, the TS value is about 366.8 in the 1 – 10 GeV band from T_0 to $T_0 + 50,000$ seconds. To obtain the detection significance, we carry out pseudo-experiments as follows. We adopt the same sky regions of the selected GRB samples but choose data

² https://user-web.icecube.wisc.edu/~grbweb_public/index.html

³ <http://fermi.gsfc.nasa.gov/ssc/data/access/lat/BackgroundModels.html>

three months after each burst, and bin the data into 50000 s bins, and re-do the same likelihood fitting to calculate the TS values of the pseudo-data. The distributions of the TS values are shown in Figure A1. We find that the TS distributions can be well fitted using the χ^2_ν distribution with degree-of-freedom ν , and get $\nu = 36.8$ and 10.1 for the two samples, respectively. According to the fitting χ^2_ν distributions, we estimate that the detection significance of GRBs is approximately 99.7σ and 17.9σ for the LAT detected and undetected samples.

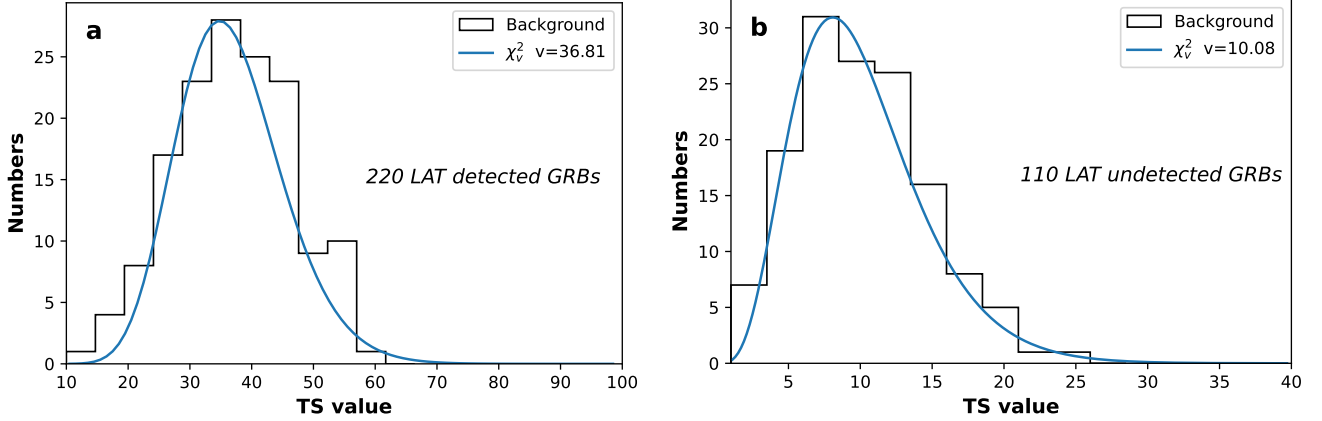


Figure A1. The distributions of TS values of pseudo-experiments, for the 220 LAT detected sample (panel a) and the 110 LAT undetected sample (panel b). The solid line in each panel is the best-fitting χ^2_ν distribution with degree-of-freedom ν .

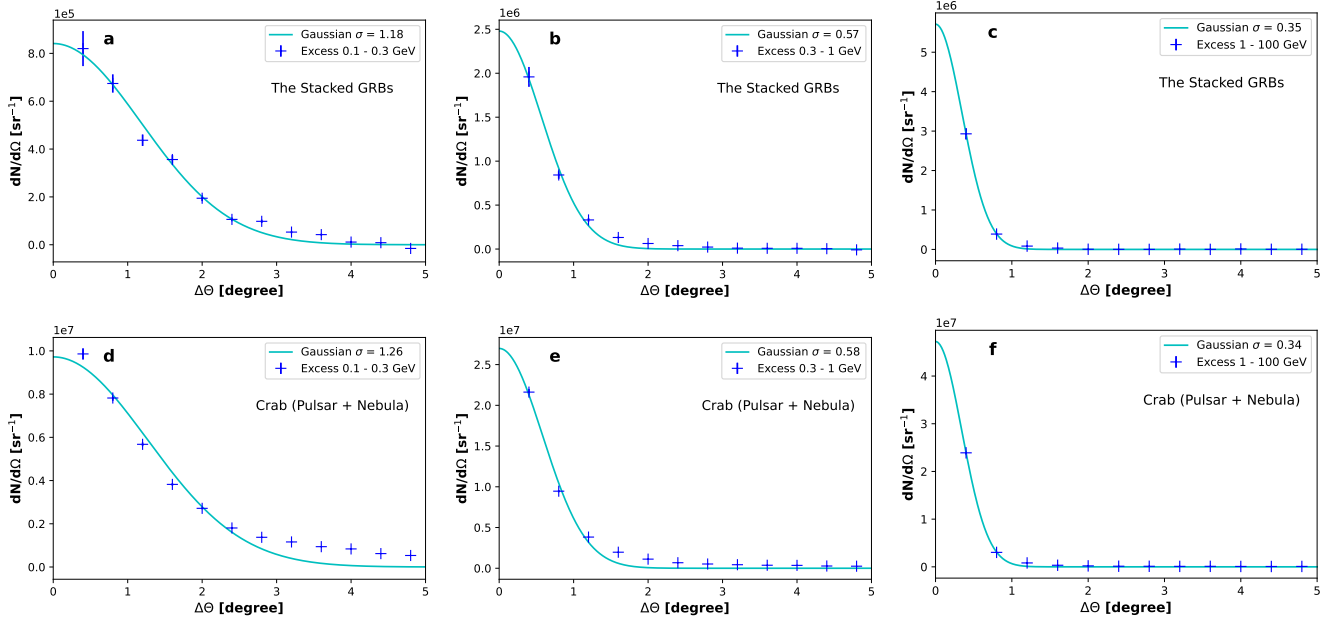


Figure A2. Angular distributions of excess photons from stacked GRBs (panels (a)-(c)) and from crab (panels (d)-(f)). Results for three energy bands, 0.1 – 0.3 GeV, 0.3 – 1 GeV, and 1 – 100 GeV, are shown. For the GRB sample, the data from T_0 to $T_0 + 50,000$ s are extracted, and for crab the data of one year observation (from August 4, 2008 to August 4, 2009) are used. The solid line in each panel shows the Gaussian fitting result.

To check whether the excess emission is consistent with a point-like source, we show the angular distributions of residual events for 3 energy bands in panels **a-c** of Figure A2, for the 220 LAT detected sample. As a comparison, the angular distributions from the crab (including both the pulsar and nebula) for the same energy bands are shown in panels **d-f**. We can see that the angular distributions of the excess emission and the crab are consistent with each other for $E > 0.3$ GeV. For the lowest energy bin, slight differences exist which may be due to different spectral shapes of them.

C. SPECTRUM ANALYSIS

The spectral energy distribution (SED) of GRBs is calculated as

$$\phi(E) = \frac{N_{\text{excess}}}{\Delta E_{\text{bin}} \Delta T A_{\text{eff}}}, \quad (\text{C1})$$

where N_{excess} represents the number of signal photons within the energy bin ΔE_{bin} and time bin ΔT . The effective area of Fermi-LAT, A_{eff} , depends on the inclination angle (θ), energy (E), and conversion types (FRONT or BACK) of incident photons. For more details one can refer to the performance⁴ of the Fermi-LAT detector. The relevant performance parameters are available in the calibration data⁵. The systematic uncertainty of the flux calculation due to the effective area is estimated to be about 5% (Ackermann et al. 2012b).

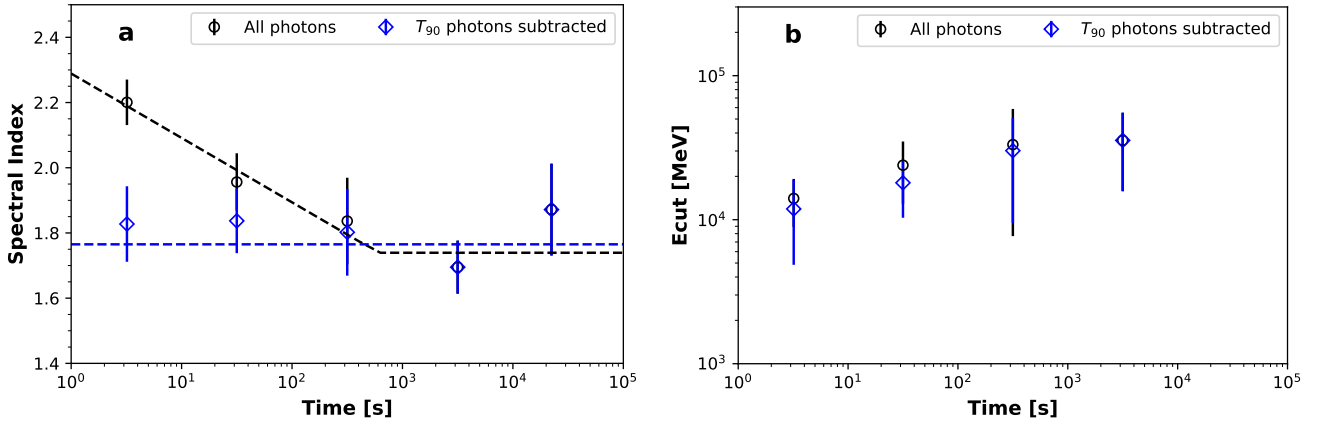


Figure A3. The evolution of the spectral index and the cutoff energy. Panels **a** and **b** track the temporal evolution of the spectral index and the cutoff energy, where black and blue points denote the values for the full and T_{90} -subtracted samples, respectively.

After getting the SED of the stacking GRBs, we use the ECPL model to fit the SED. The obtained spectral indices and cutoff energies for different data sample (including photons within T_{90} or not) and different time bin are shown in Figure A3. If all the photons are taken into account, we find that the spectral index experiences a time evolution from soft to hard. After removing photons within T_{90} , the index keeps almost unchanged with time. The cutoff energy shows a trend of increase with time. However, due to the relatively large uncertainties of the current data, we cannot draw a firm conclusion about the evolution of the spectral cutoff.

⁴ https://www.slac.stanford.edu/exp/glast/groups/canda/lat_Performance.htm

⁵ https://heasarc.gsfc.nasa.gov/FTP/caldb/data/fermi/lat/bcf/ea/aeff_lat.fits

D. LIGHT CURVES

To obtain the light curves, we bin the data into different time bins, and use a power-law (PL) model of GRBs to fit the data. For the 220 LAT detected GRBs, the light curves in two energy bands: 0.1 - 1 GeV and 1 - 100 GeV are derived. For the 110 LAT undetected GRBs, only significant emission in the 1 - 10 GeV band is found, and the light curve in this energy band is derived.

As shown in Figure 3, the light curves shows several segments of power laws. A three-piece smoothly broken power law function is employed to fit the light curves

$$\phi(t) = \phi_0 t^{\alpha_0} \left[1 + \left(\frac{t}{t_{\text{br},1}} \right)^w \right]^{-\alpha_1/w} \left[1 + \left(\frac{t}{t_{\text{br},2}} \right)^w \right]^{-\alpha_2/w}, \quad (\text{D2})$$

where w is the smoothness parameter which is fixed to be 5 in this work. For the 110 LAT undetected GRBs, the light curves at early time are not well measured due to limited number of photons, and the two-piece smoothly broken power law function is enough. Fitting parameters are presented in Table A1.

Table A1. The fitting results of the light curve parameters with 1σ uncertainties.

	Energy (GeV)	α_0	$t_{\text{br},1}$ (s)	α_1	$t_{\text{br},2}$ (s)	α_2
220 GRBs	0.1 - 1	0.67 ± 0.16	1.93 ± 3.23	0.77 ± 0.04	122.20 ± 18.10	1.62 ± 0.04
All photons	1 - 100	0.70 ± 0.50	1.06 ± 0.61	0.44 ± 0.07	104.58 ± 20.17	1.46 ± 0.04
220 GRBs	0.1 - 1	1.54 ± 0.42	1.02 ± 0.38	0.27 ± 0.04	96.91 ± 9.4	1.55 ± 0.03
T_{90} subtracted	1 - 100	1.53 ± 0.53	0.81 ± 0.23	0.20 ± 0.10	93.61 ± 16.94	1.46 ± 0.04
110 GRBs	1 - 10	-	-	0.30 ± 0.20	8598.97 ± 3155.01	3.70 ± 1.14
All photons						
110 GRBs	1 - 10	-	-	0.16 ± 0.22	8134.23 ± 3017.92	3.72 ± 1.14
T_{90} subtracted						

E. THE FORWARD SHOCK MODEL FOR GRB AFTERGLOW

We use a standard forward shock model to account for the observations of this work, speculating that high energy electrons are accelerated by shocks due to the interactions of relativistic GRB jets and the circum-burst medium (Kumar & Zhang 2015), and the broadband electromagnetic emission is produced via the synchrotron and the SSC emission processes (Meszaros & Rees 1997; Sari et al. 1998; Wang et al. 2019). In this model, the emission is determined by a set of parameter: the initial Lorentz factor Γ_0 of the jet, the initial isotropic kinetic energy E_0 , the jet opening angle θ_j , the energy partition fractions of the high-energy electrons ϵ_e and magnetic field ϵ_B , the spectral index of electrons p , the medium density profile as a function of radius $n = n_0(R/R_0)^{-k}$, and the redshift of the GRB z .

A complexity in our case is that we are treating a sample of GRBs instead of a single burst. The diversity of the burst parameters need to be taken into account. We find that the initial Lorentz factor is a sensitive parameter affecting the evolution of the afterglow. We assume a log-normal distribution of Γ_0 , with a mean value of $\log(\Gamma_0) = 2.37$ and a width of 0.26. The distribution of $\log(\Gamma_0)$ is shown in panel **a** of Figure A4, and is consistent with that given in Liang et al. (2010).

The 220 LAT detected sample represents a brighter sample in γ -ray radiation, and a larger Lorentz factor within the range of $[130, 800]$, a higher initial kinetic energy of 4×10^{53} erg, and a narrower jet opening angle of 0.8° are assumed. The initial Lorentz factor and the initial kinetic energy follows approximately the scaling relation of $\Gamma_0 \sim E_0^{0.25}$ as found in Liang et al. (2010) (see panel **b** of Figure A4). For the 110 LAT undetected sample, the Lorentz factor is restricted to the range of $[60, 250]$, the initial kinetic energy is set to be 4×10^{52} erg, and the jet opening angle is set to be 4° . The other model parameters are fixed as $n_0 = 1 \text{ cm}^{-3}$, $k = 0$, $p = 2.1$, $\epsilon_e = 0.1$, $\epsilon_B = 10^{-4}$, and $z = 1$.

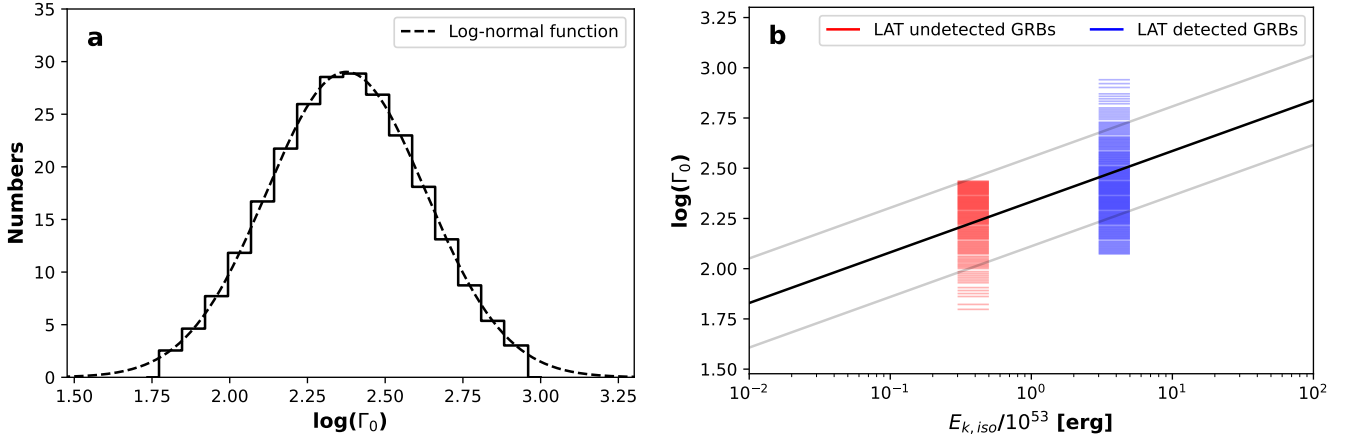


Figure A4. Lorentz factor. **a** The distribution of $\log(\Gamma_0)$ and the Gaussian fitting curve (dashed line). **b** Thick and thin lines show the $\Gamma_0 - E_0$ relation and the uncertainty ranges given in Liang et al. (2010). Shaded red and blue regions show the parameter regions adopted in the modeling of this work.

As can be seen in Figure 4, the power law index of the second segment (α_1) of the 220 LAT detected sample is determined by the cumulative effect of the GRBs with different Lorentz factors. For individual GRB, the initial Lorentz factor can be related with the peak time of the light curve as (Ghirlanda et al. 2018)

$$\Gamma_0 \approx 410(E_0/10^{54} \text{ erg})^{1/8}(n_0/\text{cm}^{-3})^{-1/8}(t_{\text{peak}}/10 \text{ s})^{-3/8}. \quad (\text{E3})$$

For the maximum Lorentz factor of 800, the peak time is about 1.2 s, which just corresponds to $t_{\text{br},1}$ of the 220 LAT detected sample. The second break at around 100 s corresponds roughly to the minimum Lorentz factors of the sample. The jet break effect when the Lorentz factor becomes smaller than $1/\theta_j$ also slightly affects the time of the second break $t_{\text{br},2}$ and the decay slope after $t_{\text{br},2}$. The jet break time can be estimated as (Wu et al. 2004)

$$t_{\text{jet}} \approx 1210 (\theta_j/1^\circ)^{8/3}(E_0/10^{54} \text{ erg})^{1/3}(n_0/\text{cm}^{-3})^{-1/3} \text{ s}. \quad (\text{E4})$$

Figure A5 show the light curves assuming that there is no jet break effect, which are inconsistent with the data at late time. Therefore, our data suggest the existence of jet breaks in general.

F. X-RAY LIGHT CURVES FROM SWIFT/XRT

The light curve of the 110 LAT undetected GRBs cannot be well explained by the above model. We expect that there might be late-time energy injection effect in the data. In this case, the light

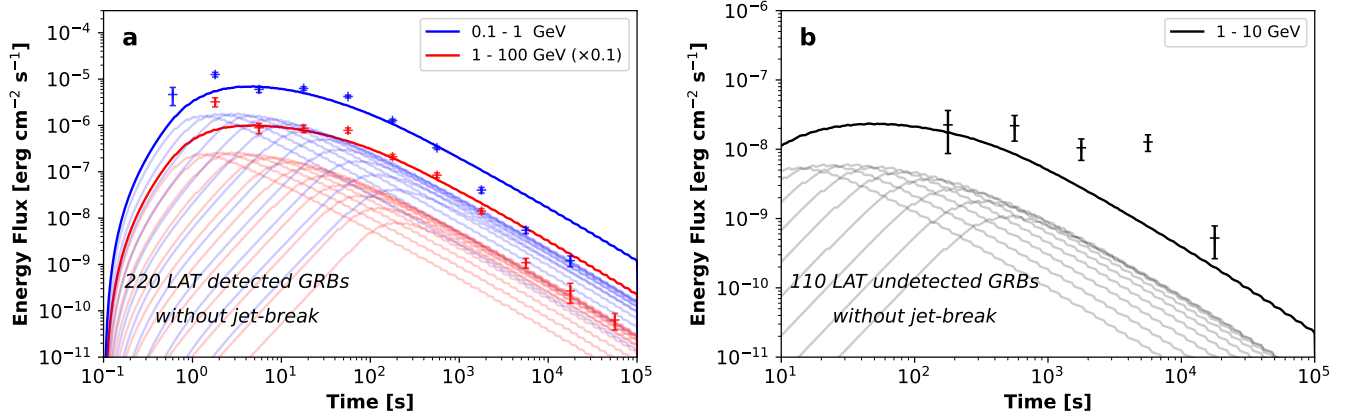


Figure A5. Stacking light curves of the GRB populations compared with the data, assuming no jet breaks. Panel **a** is for the 220 LAT detected sample, and panel **b** is for the 110 LAT undetected sample.

curve of the X-ray afterglow would show a shallower-than-normal decay behavior (Zhang et al. 2006). We therefore collect the Swift/XRT light curves of the two samples to investigate whether there are differences of their X-ray light curves.

Table A2. The classification of Swift/XRT light curves for the samples.

	No break	One break	Canonical	Oddball	TBD	None
220 LAT detected GRBs	57	11	15	15	10	112
110 LAT undetected GRBs	43	23	24	14	6	-

We classify the Swift/XRT light curves into five categories as defined in Evans et al. (2009): “No break”, “One break”, “Canonical”, “Oddball”, and cases with insufficient data (“TBD” or “None”). The results are summarized in Table A2. The categories that may be used to identify possible energy injection features include the “Canonical”, “One break”, and “Oddball” cases. It shows that 37 out of the 108 GRBs with Swift/XRT data of the 220 LAT-detected GRBs belong to these three categories, and for the 110 LAT undetected sample, 49 out of 110 belong to these three categories. The fraction is slightly higher for the 110 LAT undetected sample. We further show the slope parameters and the break time of the Swift/XRT light curves in Figure A6. In panel **a** the power-law indices α_1 and α_2 are shown, and in panel **b** the slope α_1 versus the break time are shown. Here α_1 and α_2 are the temporal decay indices before and after the break, respectively, and T_{break} is the break time (when there are multiple breaks, the parameters describe segments II and III in Zhang et al. (2006) are adopted). It can be seen that the majority of the 49 LAT undetected GRBs have $\alpha_1 < 1$, indicating that there might be energy injection processes for these GRBs. As a comparison, the 37 LAT detected GRBs have α_1 values either bigger or smaller than 1. The break time of the 49 LAT undetected GRBs are mostly within 10^3 and 10^4 s, while that of the 37 LAT detected GRBs are more broadly distributed. These properties provide support for the existence of energy injection features for the 110 LAT undetected sample.

REFERENCES

Abdalla, H., et al. 2021, *Science*, 372, 1081

Abdollahi, S., et al. 2022, *Astrophys. J. Supp.*, 260, 53

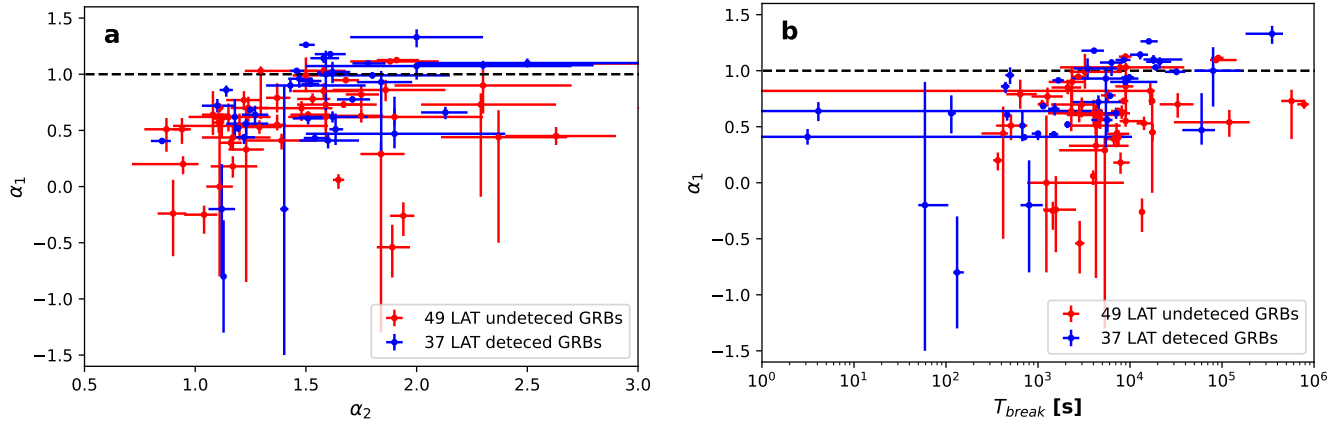


Figure A6. Statistical analysis of Swift/XRT light curves. Panel **a** shows the distributions of the two decay indices derived from the Swift/XRT light curves of the sample. Panel **b** presents the distribution of the first decay index against the subsequent break time in the Swift/XRT light curves.

- Acciari, V. A., et al. 2019a, *Nature*, 575, 459
— 2019b, *Nature*, 575, 455
Ackermann, M., et al. 2012a, *Astrophys. J.*, 750, 3
— 2012b, *Astrophys. J. Suppl.*, 203, 4
— 2014, *Science*, 343, 42
— 2015, *Astrophys. J.*, 799, 86
— 2016, *Astrophys. J.*, 822, 68
Ajello, M., et al. 2019, *Astrophys. J.*, 878, 52
Atwood, W. B., et al. 2009, *Astrophys. J.*, 697, 1071
Axelsson, M., et al. 2025, *Astrophys. J. Suppl.*, 277, 24
Cao, Z., et al. 2023, *Science*, 380, 1390
Casanova, S., Dingus, B. L., & Zhang, B. 2007, *Astrophys. J.*, 656, 306
Dermer, C. D., Chiang, J., & Mitman, K. E. 2000, *Astrophys. J.*, 537, 785
Donato, D., Angelini, L., Padgett, C. A., et al. 2012, *Astrophys. J. Suppl. Ser.*, 203, 2
Evans, P. A., et al. 2009, *Mon. Not. Roy. Astron. Soc.*, 397, 1177
Gao, H., Lei, W.-H., Zou, Y.-C., Wu, X.-F., & Zhang, B. 2013, *New Astron. Rev.*, 57, 141
Ghirlanda, G., Nappo, F., Ghisellini, G., et al. 2018, *Astron. Astrophys.*, 609, A112
Ghisellini, G., Ghirlanda, G., & Nava, L. 2010, *Mon. Not. Roy. Astron. Soc.*, 403, 926
Huber, B., Tchernin, C., Eckert, D., et al. 2013, *Astron. Astrophys.*, 560, A64
Joshi, J. C., & Razzaque, S. 2021, *Mon. Not. Roy. Astron. Soc.*, 505, 1718
Kumar, P., & Duran, R. B. 2010, *Mon. Not. Roy. Astron. Soc.*, 409, 226
Kumar, P., & Zhang, B. 2015, *Phys. Rept.*, 561, 1
Liang, E.-W., Yi, S.-x., Zhang, J., et al. 2010, *Astrophys. J.*, 725, 2209
McCann, A. 2015, *Astrophys. J.*, 804, 86
Meegan, C., et al. 2009, *Astrophys. J.*, 702, 791
Meszaros, P., & Rees, M. J. 1997, *Astrophys. J.*, 476, 232
Pan, X., Jiang, W., Yue, C., et al. 2024, *Nucl. Sci. Tech.*, 35, 149
Ravasio, M. E., Ghirlanda, G., & Ghisellini, G. 2024, *Astron. Astrophys.*, 685, A166
Rhoads, J. E. 1999, *Astrophys. J.*, 525, 737
Sari, R., & Esin, A. A. 2001, *Astrophys. J.*, 548, 787
Sari, R., Piran, T., & Narayan, R. 1998, *Astrophys. J. Lett.*, 497, L17
Wang, X.-Y., Liu, R.-Y., Zhang, H.-M., et al. 2019, *Astrophys. J.*, 884, 117
Wu, X. F., Dai, Z.-G., & Liang, E. W. 2004, *Astrophys. J.*, 615, 359
Yamazaki, R., Sato, Y., Sakamoto, T., & Serino, M. 2020, *Mon. Not. Roy. Astron. Soc.*, 494, 5259
Zhang, B., Fan, Y. Z., Dyks, J., et al. 2006, *Astrophys. J.*, 642, 354
Zhang, B., & Meszaros, P. 2001, *Astrophys. J.*, 559, 110
— 2004, *Int. J. Mod. Phys. A*, 19, 2385
Zhang, B.-B., Zhang, B., Liang, E.-W., et al. 2011, *Astrophys. J.*, 730, 141